RESEARCH ARTICLE

Intrinsic defects generated by iodine during TiO₂ crystallization and its relationship with electrical conductivity and photoactivity

Andre A. Bernardes[1] | **Andre L. da Silva**[1] | **Bruno Ramos**[1] |
Fabio C. Fonseca[2] | **Douglas Gouvêa**[1]

[1]Department of Metallurgical and Materials Engineering, Escola Politécnica—University of São Paulo, São Paulo, Brazil

[2]Instituto de Pesquisas Energéticas e Nucleares, IPEN-CNEN/SP, São Paulo, Brazil

Correspondence
Andre L. da Silva, Department of Metallurgical and Materials Engineering, Escola Politécnica—University of São Paulo, São Paulo 05508-030, Brazil.
Email: andresilva.urussanga@gmail.com

Funding information
Fundação de Amparo à Pesquisa do Estado de São Paulo, Grant/Award Numbers: 2014/50279-4, 2017/11937-4, 2019/10109-6, 2020/15230-5

Abstract

Defect formation during synthesis is one of the strategies used to improve the photoactivity of polycrystalline semiconductors such as titanium dioxide (TiO₂). Defects can modify the electronic structure of TiO₂ and change the surface of the interaction between the photocatalyst and the reactants. In this study, TiO₂ relationship between processing in the presence of iodine and the consequent formation of intrinsic defects were explored. TiO₂ nanoparticles were synthesized using the polymeric precursor method and exposed to iodine ions at concentrations up to 5 mol%. After calcination at 350°C, detailed chemical analyses revealed that iodine was absent in the samples. However, the TiO₂ properties, such as specific surface area, crystallite sizes, and specific grain boundary area, were affected. Further experiments, such as electron paramagnetic resonance, diffuse reflectance, optical measurements, and electrochemical impedance spectroscopy indicated the presence of defects in the iodine-processed samples. These defects directly influenced the electrical properties of the material, which affected the photoactivity, measured by the degradation of acetaminophen.

KEYWORDS
defect formation, electrical properties, interfacial segregation, photocatalysis, TiO₂

1 | INTRODUCTION

Crystalline defects in materials are crucial to understanding most of the materials' properties, and the development of their micro/nanostructures. Defect equilibrium in a ceramic semiconductor oxide such as TiO₂ has as main thermodynamic variables the pressure, temperature, the partial pressure of oxygen, and the concentration of impurities or additives. The defects generated by the presence of additives in these materials can modify fundamental properties such as electrical, thermal, or optical. They can also change the development of micro/nanostructures because of the modification of the chemical composition of the interfaces due to segregation or/and diffusion coefficients.[1]

Electronic or point defects in nanoxide semiconductors are generally formed by the solubility of ionic additives.[2] The general concept is that the ionic additive is soluble by substitution or interstitial in the bulk with the consequent

defect formation. However, less attention has been paid to the presence of anionic additives that are susceptible to evaporation during powder crystallization. When evaporation is accompanied by a change in the oxidation state for gas formation, there may be an oxidation/reduction of the matrix oxide species that alters the balance of intrinsic defects.

The introduction of defects in semiconductors such as TiO_2 is relevant in applications such as catalysis, photocatalysis, and electrophotocatalysis. Defects can influence catalytic processes by modifying the electronic structure of TiO_2 and altering the interaction between the surface of the catalyst and the reactants.

Besides these traditional approaches to how defects alter the electronic structure of the material, one relevant aspect of photocatalysis that has been ignored is the electrical conductivity across grain boundaries (GBs). When an additive segregates in the GBs, it can modify the electrical conductivity of the material.[3] This is a consequence of the modification of the electrical potential barrier height and the activation energy for conduction. Therefore, the GBs are expected to act as shortcuts for charge transport, while the electrical conductivity of the polycrystalline species tends to increase with the GB density.

This work aims to study the formation of intrinsic defects in TiO_2 nanoparticles caused by the introduction of iodine during synthesis. The defects were detected by color measurements using the CIE L*a*b system, UV–vis diffuse reflectance, electron paramagnetic resonance spectroscopy, and diffuse reflectance infrared Fourier transform (DRIFT) spectroscopy. Then, we used electrochemical impedance spectroscopy (EIS) to measure the overall conductivity of the system, especially at the grain boundary regions. Finally, we studied the photoactivity of the system by degradation of acetaminophen. The goal is to unravel the interdependence between GB electrical conductivity and the photocatalytic properties of nanostructured TiO_2.

2 | EXPERIMENTAL METHODS

2.1 | Synthesis of TiO_2 nanopowders in the presence of iodine

TiO_2 nanopowders were synthesized using the polymeric precursor method. The iodine target molar concentrations during processing were 0.00, 0.05, 0.10, 0.50, 1.00, 2.50, and 5.00 mol%. The titanium-based polymeric precursor was prepared by adding titanium isopropoxide (19.4 wt%) to ethylene glycol (45.4 wt%) at 40°C with constant stirring. After heating the mixture to 70°C, citric acid (35.2 wt%) was added, followed by heating to 120°C for 30 min for polyesterification. The resin was saved, and a

thermogravimetric experiment at 900°C for 5 h was performed to determine its yield, which was ~6%. Iodine was introduced by adding an appropriate amount of an aqueous NH_4I solution (0.1 mol L^{-1}) to the resin. Each composition was mixed for 30 min in an individual container, followed by calcination.

Calcination was carried out in two steps. First, to decompose and eliminate organic traces, each sample was held at 350°C for 4 h. Thus, the samples were ground with a mortar and pestle and heated to 350°C for 15 h under air flow to complete the reaction and stabilize the particle size.

2.2 | Powder characterization

XRD patterns were obtained using an X'Pert PRO PW 3040/00 Philips diffractometer with Cu Kα radiation, operated at 45 kV and 40 mA. The step size was set at 0.02°, with a step time of 50 s in the 2.5°−90° 2θ range. Crystallite sizes and lattice parameters were calculated by Rietveld analysis using X'Pert Highscore software with $MgAl_2O_4$ as a standard obtained under the same conditions as the TiO_2 samples. The peak profile used to refine the diffractograms was described by the pseudo-Voigt function, without asymmetry correction, and the FWHM parameters were refined using the Caglioti function.

The specific surface areas of the samples were determined by the adsorption of N_2 gas at 77 K (Micromeritics Gemini III 2375 Surface Area Analyzer) according to the Brunauer-Emmett-Teller (BET) method. Before the experiment, the samples were subjected to thermal pretreatment at 300°C for ~16 h (100 mmHg—Micromeritics VacPrep 061) for surface degassing.

Powder density measurements were carried out by helium gas pycnometry using a Micromeritics AccuPyc II 1340 pycnometer after 200 purges. Before the experiments, the samples were dried at 105°C for 12 h.

The chemical composition of the powders was determined by X-ray fluorescence spectroscopy (XRF) using a Malvern Panalytical Zetium XRF spectrometer. The iodine concentration was measured using a HI 4111 iodide ion-selective electrode (ISE) connected to a pH Analyzer 300 M. The samples were dissolved in an aqueous sulfuric acid solution (50.0% in volume) and the pH was neutralized with sodium hydroxide. The selective lixiviation method[4,5] was also employed to try to detect iodine on the surface of the samples. The iodine concentration in samples was also visualized by energy-dispersive X-ray spectroscopy (EDS) using an FEI Inspect F50 FEG scanning electron microscope (SEM), operated at 20 kV and 122.7 eV resolution.

TiO_2 defects were identified by electron paramagnetic resonance spectroscopy (EPR). A Bruker EMX electronic

paramagnetic resonance spectrometer was used, operated at 150 K, controlled by a Bruker BVT-2000 system with a microwave frequency of 9.498 GHz, and magnetic field range (B0) measured from 3280 to 3480 Gauss.

Diffuse reflectance infrared Fourier transform (DRIFT) spectroscopy was performed using the Thermo-Nicolet Magna 560 spectrometer with a scanning capacity of $400-4000$ cm^{-1} and a resolution of 4 cm^{-1}.

X-ray photoelectron spectroscopy (XPS) measurements were performed using a modular ultrahigh vacuum system (UNI-SPECS UHV Surface Analysis System) equipped with XPS. The Al Kα line (hν = 1254.6 eV) was used as the ionization source and the atomic percentage composition of the surface layer (< 5 nm) was determined by the relative proportions of the peak areas corrected by the Scofield atomic sensitivity factors, with a precision of $\pm 5\%$. The spectra were deconvoluted using a Voigtiana-type function, with Gaussian (70%) and Lorentzian (30%) combinations.

For color measurements, the TiO$_2$ nanopowders were pressed into a 20 mm × 50 mm rectangular matrix using a Carver hydraulic press at 0.3 ton cm^{-2} followed by the analysis on a MiniScan XE Plus equipment by the CIE L*a*b* system and standard illuminant D65.

Electrochemical impedance spectroscopy (EIS) was performed on TiO$_2$ samples processed with 0.00, 1.00, and 5.00 mol% iodine using a SI 1260 / gain-phase analyzer (Solartron) impedance meter connected to a closed furnace with controlled temperature and atmosphere. The EIS data were collected in the frequency range of 30 MHz to 1 Hz with an AC voltage amplitude of 500 mV and without dc bias. Before the experiments, the samples were presintered at 360°C for 1 h and the experiments were carried out from 20°C to 125°C.

The photoactivity of the samples was evaluated by the degradation of the model contaminant acetaminophen (ACT) using an aqueous TiO$_2$ suspension containing ~10 mg of photocatalyst in 8 mL of a 5 ppm ACT solution. The suspension was irradiated with a monochromatic UV-A LED (LG, λ = 370 nm), which provided an irradiance of 7 mW cm^{-2} on the reactor walls. Before the light was turned on, the samples were stirred using a magnetic stirrer at ~25°C for 30 min to reach an equilibrium of adsorption and desorption of ACT molecules on the TiO$_2$ surface. During the test, the UV-A LED was the only source of light in the room, eliminating any possible interference of other types of light with the reaction kinetics. Aliquots of the suspension were collected every 15 min and filtered to eliminate any type of contamination by solid particles of the photocatalyst. The aliquots used during the photocatalytic test were 100 μL each, resulting in a total volume of 900 μL after the test, which accounted for approximately 10% of the total volume used in the

experiment. During the test, the system was continuously mixed to ensure uniform dispersion of the catalyst, maintaining a constant catalyst concentration in the remaining volume. The concentration of ACT in the aliquots was measured by high-performance liquid chromatography (HPLC) with UV detection at 243 nm (Lc20-A, Shimadzu Co.) after elution through a C18 column with a 0.8 mL min^{-1} isocratic flow of methanol and deionized water in a proportion of 1:3.

3 | RESULTS AND DISCUSSIONS

Chemical analyses were performed to investigate the chemical elements present in the samples. EDS analysis revealed that there were no iodine peaks in iodine-processed TiO$_2$ (3.937 keV, Figure S1). The only elements identified were O, Ti, and Au (2.120 keV), the latter due to the coating used for the analysis. To double-check the EDS results, an iodide-selective electrode (ISE) was employed. First, the TiO$_2$ samples were dissolved in an aqueous sulfuric acid solution (50.0% in volume), then, to reach the pH working range (2.00 to 11.00) of the ISE, the solution was neutralized with sodium hydroxide. No iodide was detected, which confirmed the EDS results. The powders were also leached by the selective lixiviation process, and the supernatant was analyzed by ISE. No iodine was detected, which also confirms the EDS results. Possibly, the ammonium iodide used as an iodine precursor during the synthesis process dissociated into ammonia and iodine gas and evaporated during the reaction.[6]

Although the chemical analyses did not show the presence of iodine in the samples, an investigation was conducted to evaluate the potential effects left by the processing in the presence of iodine. The main characterizations were color measurements, UV–vis diffuse reflectance, EPR, XPS, electrochemical impedance spectroscopy, and photoactivity.

Figure 1 shows the X-ray diffractogram for samples processed in the presence of iodine in concentrations ranging from 0.00 to 5.00 mol%. The predominant phase is anatase, but a small peak of rutile ($2\theta = \sim27°$) can also be observed in some samples. Because the peaks are too small, it was not possible to quantify them in the phase volume. The broad peaks observed are typical of nanostructured materials.

The crystallite sizes, specific surface area (SSA), density, specific grain boundary (SGB) area, and SGB/SSA ratio are listed in Table 1. Crystallite size (D) and pycnometry density (ρ) were used to calculate the SGB and the total specific interface area (TIA). The former was calculated using Equation (1) by assuming that all particles had a tetrakaidecahedral shape. The latter was calculated

TABLE 1   Crystallite sizes, specific surface area (SSA), density, specific grain boundary (SGB) area, and SGB/SSA ratio of iodine-processed TiO_2.

Samples	Crystallite size (nm)	SSA ($m^2 g^{-1}$)	Density ($g cm^{-3}$)	SGB ($m^2 g^{-1}$)	SGB/SSA
0.00%	13.5 ± 0.1	60.9 ± 0.1	3.444 ± 0.005	46.1 ± 0.3	0.76
0.05%	13.7 ± 0.1	58.5 ± 0.1	3.465 ± 0.006	45.6 ± 0.4	0.78
0.10%	14.1 ± 0.1	57.3 ± 0.1	3.469 ± 0.007	44.1 ± 0.4	0.77
0.50%	14.7 ± 0.1	57.5 ± 0.1	3.487 ± 0.008	40.5 ± 0.4	0.70
1.00%	11.7 ± 0.1	62.6 ± 0.1	3.446 ± 0.007	56.9 ± 0.4	0.91
2.50%	12.9 ± 0.1	57.9 ± 0.1	3.505 ± 0.013	49.3 ± 0.4	0.85
5.00%	11.3 ± 0.1	49.9 ± 0.1	3.432 ± 0.005	66.3 ± 0.5	1.33
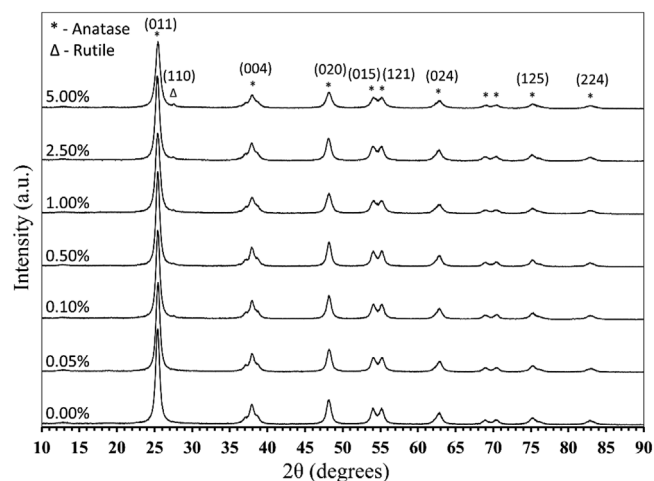
FIGURE 1   X-ray diffractograms of iodine-processed TiO_2 samples.

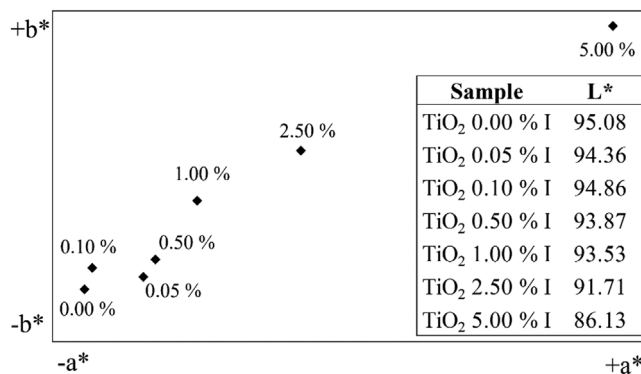**FIGURE 2**   CIE L*a*b* color system showing the color change in iodine-processed TiO_2 samples.

according to Equation (2) considering that each grain boundary was shared by two particles.

$$TIA = \frac{7.1}{\rho D}, \tag{1}$$

$$SGB = \frac{TIA - SSA}{2}. \tag{2}$$

The crystallite sizes were slightly affected by the presence of iodine during the synthesis. They increased for samples from 0.00 to 0.50 mol% iodine, and then dropped to values below the pristine TiO_2. The SSAs did not present any specific trend and can be better analyzed together with the SGB and the SGB/SSA ratio. The SGB showed a tendency toward higher values. The SGB/SSA ratio increased especially for TiO_2 samples processed with 1.00 and 5.00 mol% iodine. These results indicate that the presence of iodine during synthesis can affect the stability of the interfaces in this system, stabilizing the GB against the surface.[7]

The color measurements shown in Figure 2 indicate that the color of the samples changed with the amount of iodine

during synthesis. The CIE L*a*b* system shows a tendency toward the orange color (positive a and b) with a darker tonality (lower L). The change in sample color confirmed that the TiO_2 samples contained many defects.[8] Among the several color-changing mechanisms that may influence the materials optical properties, oxides are usually affected by three main mechanisms: color change because of the charge transfer between ions and defects, color change deriving from the band theory in semiconductors, with the introduction of a donor or acceptor level in the band gap by defects, and the presence of color centers generated by electrons transfer from the semiconductor lattice to defects on the surface.[9] To better understand the reasons why the color of the samples changed, the band gap of the samples using UV–vis diffuse reflectance measurements was investigated.

The UV–vis diffuse reflectance spectra are shown in Figure 3. As expected for the TiO_2 anatase phase, the samples showed a low UV reflectance between 5.0 and ~3.2 eV, and high visible reflectance at energies lower than ~3.1 eV. The reflectance decreased in the visible spectrum at wavelengths close to violet and blue, mainly for TiO_2 processed with 1.00, 2.50, and 5.00 mol% iodine. These results suggest that the TiO_2 samples absorbed light at these wavelengths,

FIGURE 3 Diffuse reflectance spectra.
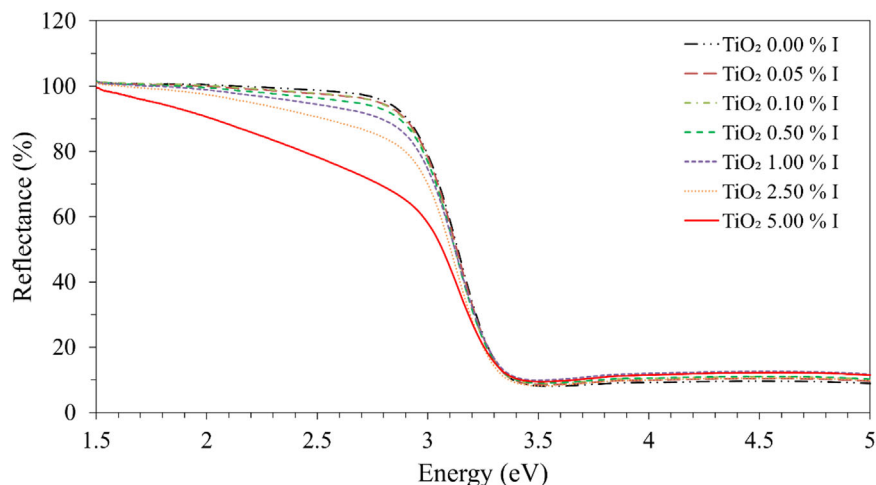
TABLE 2 TiO$_2$ band gap obtained by the Tauc method.

Sample	Band gap (eV)
TiO$_2$ 0.00% I	3.11 ± 0.03
TiO$_2$ 0.05% I	3.10 ± 0.03
TiO$_2$ 0.10% I	3.09 ± 0.03
TiO$_2$ 0.50% I	3.08 ± 0.03
TiO$_2$ 1.00% I	3.09 ± 0.03
TiO$_2$ 2.50% I	3.08 ± 0.03
TiO$_2$ 5.00% I	3.07 ± 0.03

which was observed in the material through the color variations from white to orange/yellow, and complementary colors of violet/blue, confirmed by the colorimetry results.

The band gap of the samples was estimated by applying the Kubelka–Munk function using the Tauc model in the diffuse reflectance spectra. The results are shown in Table 2. Although the band-gap values tended to decrease, they were all virtually equal, suggesting that processing did not affect the energy gap of the samples. Therefore, the color change seen in Figures 2 and 3 was not due to the narrowing of the material band gap or the creation of intermediate energy levels in the CB.

For the TiO$_2$ 5.00% I sample to obtain an orange color, its band gap should be approximately 2.60 eV, not 3.07 eV. Possibly, the interface defects that were acting as adsorption sites were also generating color centers. Color centers occur in the material when a hole-generating species, A, coexists with an electron-receiving species, B. Upon absorbing energy, the hole-generating species will eject an electron to the electron-receiving species, for example, an oxygen vacancy, forming an A$^+$ center and a B$^-$ center, also known as F-center (F, F$^+$, F^{++}, and Ti^{3+}). For this electronic transition to occur, light absorption is necessary, often in the visible spectrum, which makes a colorless material obtain color.[9] Serpone[10] suggests that visible light absorption by doped TiO$_2$ does not occur by narrowing
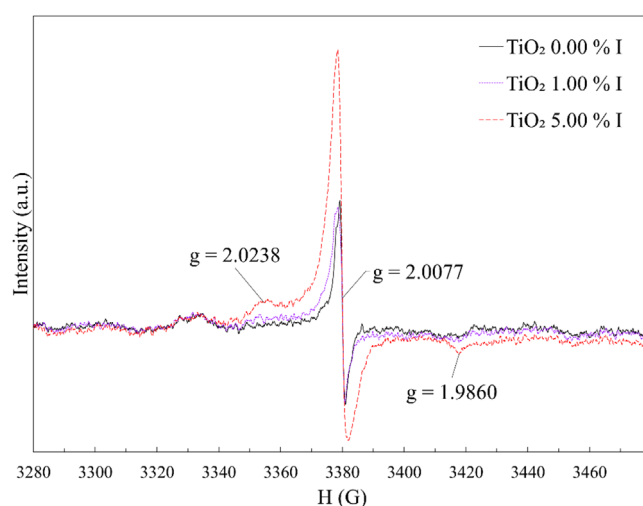
FIGURE 4 EPR spectra for TiO$_2$ 0.00% I, TiO$_2$ 1.00% I, and TiO$_2$ 5.00% I samples.

the band gap or creating intermediate energy levels in the semiconductor. This is due to the generation of defects that act as color centers that absorb the visible spectrum. Moreover, manipulation of the band gap through doping is a known phenomenon, but it requires a large amount of dopant, which can drastically modify the chemical composition of the photocatalyst and form new crystalline phases.

Following the experiments to identify the type of defects created by iodine processing in TiO$_2$, EPR measurements were performed. Oxygen vacancies can trap unpaired electrons from the material, being detectable by EPR, while Ti^{3+} sites are paramagnetic and are usually associated with the removal of oxygen atoms from the lattice. The EPR *g*-tensor values for Ti^{3+} are in the 1.99-1.96 range. Figure 4 shows the EPR spectra of the TiO$_2$ 0.00% I, TiO$_2$ 1.00% I, and TiO$_2$ 5.00% I samples. The g-tensor values were identified at 2.0077 for all samples and at 1.9860 and 2.0238 for TiO$_2$ 5.00% I. These values can be associated with oxygen

vacancies or Ti^{3+} defects. Studies have shown that Ti^{3+} in regular positions of the anatase lattice, generated by the compensation of an extra charge carried by a cation (e.g., Nb^{5+}) or an anion (e.g., F^-) as dopants, exhibits axial EPR signals in $g = g_{xx} = g_{yy} = 1.992$ and $g_\parallel = g_{zz} = 1.962$ for spectra recorded at 10 and 77 K. The same signal appears in reduced anatase annealed under vacuum.[11] Although the signal in Figure 4 has the same axial shape, the *g*-factor values are slightly different from those reported in the literature. Similar signals have been observed in doped anatase,[11] anatase under irradiation,[12] or after thermal treatments.[13]

In most cases, defects are identified after UV or visible light irradiation. In this study, EPR measurements were performed in a closed sample holder without any illumination, further indicating that defects were generated during the synthesis as a result of iodine evaporation and that the process method influenced the formation of defects in the material. This feature agrees with previous findings of electron holes induced by valence change (O^-) identified by EPR in anatase.[12] Electron holes trapped onto an O^{2-} ion have g values between $g = 2.003$ and $g = 2.027$. The same values were obtained for anatase under illumination.

A similar result was found by Li et al.,[14] where g-factor values of $g_{zz} = 2.023$, $g_{yy} = 2.006$, and $g_{xx} = 1.987$ of an orthorhombic EPR signal were detected for N-doped TiO_2. These signals were attributed to O_2^- species generated from the interaction of atmospheric O_2 molecules with the localized electrons in the oxygen vacancies on the surface. Although these signals do not directly represent oxygen vacancies, they are indicative of the presence of paramagnetic species and probably the existence of Ti^{3+} in the lattice. The presence of O_2^- species on the surface of TiO_2 is consistent with other reports.[15] The formation of O_2^- groups on the surface of reducible oxides is possible when oxygen adsorption occurs after a preliminary reductive treatment (e.g., chemical reduction). If the electrons occupying donor levels in the band gap of a reduced oxide are excited to the conduction band, they can be transferred toward adsorbed oxygen even at low temperatures (e.g., room temperature). Electron transfer causes a depletion of charges in the conduction band, leading to a decrease in the material conductivity.[16]

To investigate the chemical states of the samples, measurements of I 3d, Ti 2p, O 1s, and C 1s were performed on TiO_2 5.00% I sample using XPS. The analysis revealed the presence of Ti, O, and C located in the binding energies of 458.25 eV, 529.50 eV, and 285.00 eV, respectively. The spectra can be seen in Figure 5. The $Ti\ 2p_{3/2}$ and $Ti\ 2p_{1/2}$ spectra are associated with TiO_2 bonds.[17] Ti^{3+} peaks, usually detected around 457.2 eV ($Ti\ 2p_{3/2}$) and 462.9 eV ($Ti\ 2p_{1/2}$), were not observed in any sample.[18–20] The main component in the oxygen spectrum was related

TABLE 3 Chemical groups of TiO_2 and iodine-processed TiO_2 DRIFT spectra, and their respective vibration bands.

Chemical group	ν (cm^{-1})	References
OH	3700–2700	21, 22
O = C = O	2350	23–25
CO	2285	25
CO	2215	25
OH	1621	21
b-CO_3^{2-} bidentate	1556	22, 25–26
Carbonates	1356–1377	23, 25
Ti—O	650–1100	21

to O-Ti bonds. Surface hydroxyl groups and oxidated carbon groups were also identified. The main component in the carbon spectrum was related to hydrocarbon groups (CH) on the surface and other oxidized carbon groups at a lower content. No iodine 3d peaks were detected, which corroborates the EDS results.

DRIFT analyses were performed to identify the species adsorbed on the surface of TiO_2 samples and their relationship with defects. The results are shown in Figure S2 and the chemical groups are presented in Table 3.

DFT and experimental studies have shown that CO_2 adsorption, activation, and dissociation processes are significantly influenced by the distribution of defects on the TiO_2 surface, as well as the phases present in the material. These studies indicate that electrons trapped in photocatalyst defects can induce the formation of CO_2^- and its subsequent dissociation into CO in the dark.[27,28] In situ DRIFT studies also confirmed that CO_2 can spontaneously dissociate into CO in reduced Rh/TiO_{2-x}[29] and $Cu(I)/TiO_{2-x}$ (P25) systems due to surface defects,[30] even without UV–vis irradiation. In these studies, exposure of photocatalyst surface defects to CO_2 led to the formation of CO_2^- species bonded to the Ti^{4+} surface site, which was detected by DRIFT in the vibration bands of 1673 and 1248 cm^{-1}. This fact suggests that adsorbed CO_2 can be activated by the spontaneous migration of excess electrons trapped in defects, such as Ti^{3+} or oxygen vacancies.[31] The CO_2 species in angular vibration mode present DRIFT bands at 1673 and 1248 cm^{-1} and are adsorbed at Ti^{3+} sites on the surface.[30] These groups were not identified in the TiO_2 samples in the present study, suggesting that the reduction of CO_2 to CO_2^- does not occur spontaneously in this system.

Figure 6 shows the electrochemical impedance spectra obtained at 20°C for TiO_2 0.00% I, TiO_2 1.00% I, and TiO_2 5.00% I samples. Each curve can be divided into two parts: one at high frequency (from ~10 MHz to 100 Hz), characterizing the electrical properties of the samples and a spike at low frequency (< 100 Hz) related to electrode
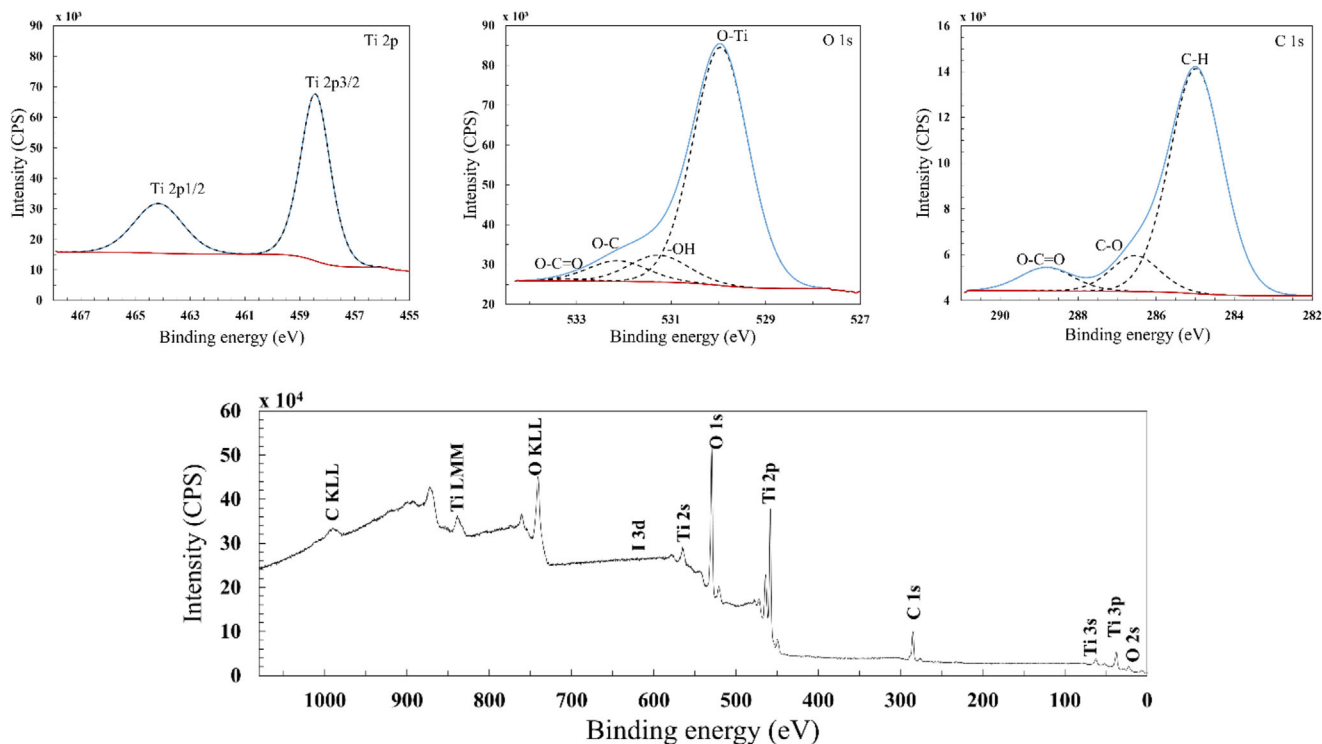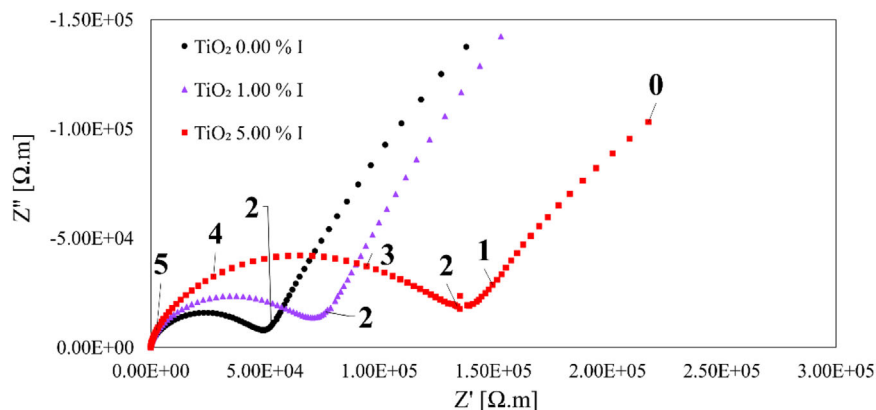
FIGURE 5 XPS spectra of Ti 2p, O 1s, and C 1s of TiO$_2$ 5.00% I. I 3d and Ti^{3+} were not detected.

FIGURE 6 Electrochemical impedance spectra showing the increase in electrical resistance for iodine-processed samples. The numbers on the curve are the logarithms of the measuring frequency, in Hertz.

reactions. The high-frequency portion of the diagrams was deconvoluted and extrapolated to find their interception with the real axis Z', which represents the total resistivity of the samples. It was observed that both capacitance and resistivity increased with the amount of iodine during the synthesis. Generally, TiO$_2$ is recognized as an n-type semiconductor at room temperature due to the presence of oxygen vacancies and interstitial titanium atoms that supply electrons to the conduction band.[32] More recently, p-type conductivity has been obtained at room temperature for undoped TiO$_2$.[33,34] This transition from n-type to p-type semiconductor occurs through the formation of titanium vacancies (electron acceptor defect), which can be generated from rutile oxidation at high temperatures

($\sim$1000°C),[33] and also from the solvothermal synthesis of anatase followed by calcination at 470°C.[34]

A possible effect for the increase in electrical resistance for iodine-processed samples is based on the presence of Ti^{3+} species segregated at the grain boundaries of the material. The EPR results (Figure 4) indicated the presence of oxygen vacancies and Ti^{3+} in the TiO$_2$ samples. When oxygen vacancies are generated, the formation of Ti^{3+} species occurs to maintain charge neutrality. However, the Ti^{3+} species were not identified by XPS on the surface of the material, suggesting that it is soluble in the bulk or at the grain boundaries. The increase in the SGB/SSA ratio (Table 1) for samples processed with iodine indicates the presence of species segregated at grain boundaries,

TABLE 4 Possible chemical reactions of ACT degradation by oxidation[43] (e_{CB}^- is the electron in the conduction band and h_{VB}^+ is the hole in the valence band).

$TiO_2 + h\nu_{UV} \rightarrow e_{CB}^- + h_{VB}^+$	(4)
$e_{CB}^- + h_{VB}^+ \rightarrow h\nu_{IR}$ (recombination)	(5)
$H_2O + h_{VB}^+ \rightarrow OH\cdot + H^+$	(6)
$OH^- + h_{VB}^+ \rightarrow OH\cdot$	(7)
$e_{CB}^- + O_2 \rightarrow O_2^-$	(8)
$ACT + h_{VB}^+ \rightarrow oxidation$	(9)
$ACT + OH\cdot \rightarrow oxidation$	(10)

which change the chemical composition and stabilize this interface.[3,35,36] The SGB/SSA ratio ranges from 0.76 to 1.33 for samples prepared with 0.00 and 5.00% iodine, respectively. As iodine was not identified during chemical analyses, the species segregated in GBs may be Ti^{3+} ions that received an electron during I_2 evaporation, with a simultaneous formation of an oxygen vacancy, as shown in Equation (3):

$$2I_O^\cdot + 2Ti_{Ti}^x\ TiO_2 \rightarrow \frac{1}{2}I_{2(g)} + 2V_O^{\cdot\cdot} + 2Ti_{Ti(GB)}^\prime \quad (3)$$
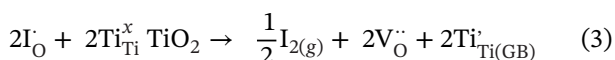
Studies have shown that the segregation of defects and electrons occurs in the GBs of TiO_2 and contributes to the increase in the potential barrier and the depletion layer at the grain boundary, influencing the conductivity of the material.[37–39] EPR spectra of anatase samples with and without grain boundaries suggest that Ti^{3+} is associated with the sublayer as it is not affected by surface adsorption, indicating that the titanium defect is located at the solid-solid interface.[40] However, oxygen vacancies are generated on the surfaces and adsorb molecular oxygen from the gas phase (or soluble in water), generating paramagnetic species that can be analyzed by EPR[41] and are related to the photocatalytic activity of TiO_2 anatase.[42]

Photodegradation of acetaminophen (ACT) was performed for TiO_2 0.00% I, TiO_2 1.00% I, and TiO_2 5.00% I samples under UV radiation to understand the contribution of defects and interfaces in anatase photoactivity. The possible chemical reactions of ACT degradation can be represented by the equations presented in Table 4.

Some steps are fundamental for the success of the ACT oxidation reaction, among them, the formation of the electron/hole pair and its recombination, the reaction of charges with molecules adsorbed on the TiO_2 surface, either water or hydroxyls, or even molecular oxygen. Note that the transfer of electrical charges occurs through sites on the surface, which are usually crystalline defects, such as oxygen vacancies.

The results displayed as the concentration of ACT over time are shown in Figure 7. Although no iodine was
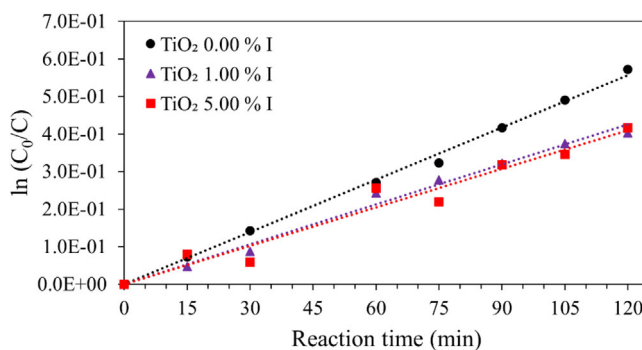

FIGURE 7 Kinetics of acetaminophen photodegradation under UV light of 370 nm wavelength.

TABLE 5 Summary of photocatalysis results.

Sample	Apparent pseudo-first order rate (min^{-1})	Specific conversion at 120 min (μmol ACT m^{-2})
TiO_2 0.00% I	4.64×10^{-3}	0.188
TiO_2 1.00% I	3.54×10^{-3}	0.139
TiO_2 5.00% I	3.41×10^{-3}	0.181

detected in the samples, the presence of defects hinders the photodegradation reaction, as evidenced by the higher apparent kinetics of decomposition seen for the TiO_2 0.00% I sample.

The term $\ln(C_0/C)$ was used to calculate a pseudo-first order reaction rate constant. Moreover, the conversion achieved at 120 min was divided by the initial specific surface area of each composition to provide a normalization of the photocatalytic degradation capacity to account for differences in surface area. These parameters are summarized in Table 5.

The lower photoactivity of the iodine-processed samples is not a result of the change in SSA, since the SSA of the TiO_2 1.00% I sample is greater than that of the TiO_2 0.00% I sample (Table 1). However, increasing the GBA (Table 1) can contribute to charge recombination by modifying the mean free path of electrons and holes or by promoting a region of charge recombination at the grain boundaries.[44] Another consideration is that the total number of defects is almost the same for both samples, as demonstrated by EPR measurements (Figure 4). Therefore, the increase in grain boundary resistivity (Figure 6) can be associated with the poor efficiency of the photodegradation reaction.

By comparing TiO_2 5.00% I with the pristine TiO_2 and TiO_2 1.00% I samples, a strong reduction in SSA simultaneously with the increase in GBA and the intensification of electrical resistance is observed (Table 1, Figures 6 and 7). In this case, an even lower photocatalytic activity was expected. However, the ACT photodegradation for
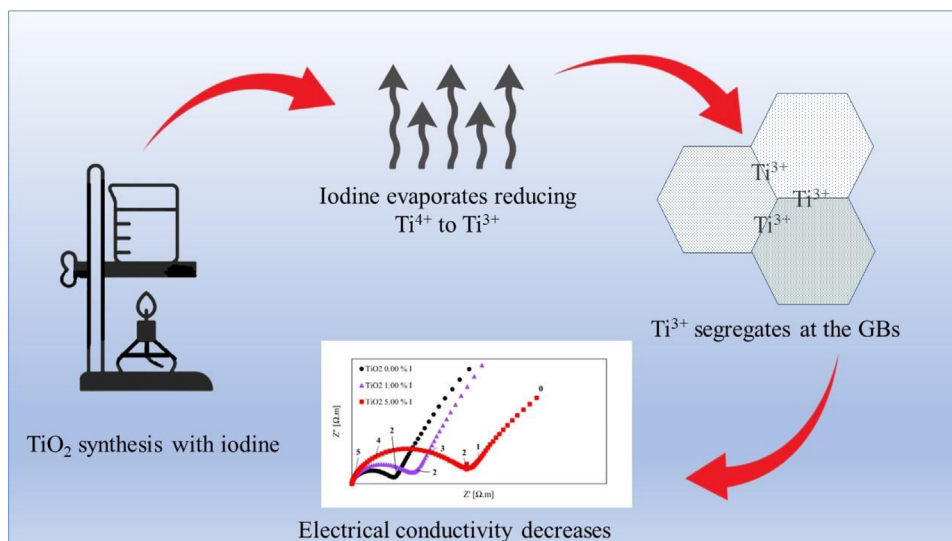
FIGURE 8 Summary of the article designated for the graphical table of contents.

the TiO$_2$ 5.00% I sample is very similar to that of the TiO$_2$ 1.00% I sample. The observed efficiency can be justified by the sharp increase in the number of defects detected by the EPR analysis (Figure 4), which could be associated with surface defects. Hence, although there is a decrease in degradation efficiency due to the increase in the grain boundary electrical resistance and the decrease in SSA, the increase in the number of defects seems to partially compensate for those effects and increase photoreactivity.

4 | SUMMARY

Intrinsic defects were formed in TiO$_2$ nanoparticles synthesized in the presence of iodine. The iodine ions evaporate during calcination and promote the reduction of Ti^{4+} to Ti^{3+}, which segregates at the grain boundaries (GBs), stabilizing this interface regarding the surface. The Ti^{3+} species segregated in the GBs decrease the overall electrical conductivity of the system, reducing the photodegradation of acetaminophen in an aqueous solution under UV irradiation (Figure 8).

5 | CONCLUSIONS

TiO$_2$ nanoparticles were processed in the presence of iodine as an additive up to 5 mol%. The results indicated that the photocatalytic activity is limited by the electrical conductivity in polycrystalline TiO$_2$. Experimental data indicate that Ti^{3+} species, probably generated by I$_2$ formation, segregate at the GBs and decrease the overall electrical conductivity of the system, reducing the photodegradation of acetaminophen in an aqueous solution under UV irradiation. The iodine ions evaporation promoted the reduction of Ti^{4+} to Ti^{3+}, which segregate at the GBs, stabilizing this interface regarding the surface. These results can be used as a guideline to design catalysts with better properties by controlling doping and dopant segregation that favor the formation of active surface species for photocatalytic reactions that are not hindered by low grain boundary electrical conductivity.

CONFLICT OF INTEREST STATEMENT
The authors declare that they have no known competing financial interests or personal relationships that could have appeared to influence the work reported in this paper.

ORCID
Andre A. Bernardes https://orcid.org/0000-0003-2108-9713

Andre L. da Silva https://orcid.org/0000-0001-8006-8870

Fabio C. Fonseca https://orcid.org/0000-0003-0708-2021

Douglas Gouvêa https://orcid.org/0000-0003-3607-8793

REFERENCES

1. Neves DCOS, da Silva AL, de Oliveira Romano RC, Gouvêa D. Fe_2O_3-doped SnO_2 membranes with enhanced mechanical resistance for ultrafiltration application. J Eur Ceram Soc. 2020;40(15):5959–66. Available from: https://doi.org/10.1016/j.jeurceramsoc.2020.06.077

2. Han L, Zou Y, Liu J, Jia B, Liu G, Ma X, et al. Effect of intrinsic point defects on the electronic and optical properties of Ho:BYF crystal. Opt Mater (Amst). 2021;121:111514. Available from: https://doi.org/10.1016/j.optmat.2021.111514

3. Fortes GM, da Silva AL, Caliman LB, Fonseca FC, Gouvêa D. Interfacial segregation in Cl^--doped nano-ZnO polycrystalline semiconductors and its effect on electrical properties. Ceram Int. 2021;47:24860–7. Available from: https://doi.org/10.1016/j.ceramint.2021.05.212

4. Gouvêa D, do Rosário DCC, Caliman LB. Surface and grain-boundary excess of ZnO-doped SnO_2 nanopowders by the selective lixiviation method. J Am Ceram Soc. 2017;100(9):4331–40. Available from: https://doi.org/10.1111/jace.14973

5. da Silva AL, Bettini J, Bernardes AA, Castro RHR, Gouvêa D. Improving TiO_2 anatase nanostability via interface segregation: the role of the ionic radius. J Phys Chem C. 2023;127(3):1536–47. https://doi.org/10.1021/acs.jpcc.2c04271

6. Lyday PA, Kaiho T. Iodine and iodine compounds. In: Wiley-VCH, editor. Ullmann's Encyclopedia of Industrial Chemistry. Wiley-VCH Verlag GmbH & Co. KGaA, Weinheim; 2015:1–13. https://doi.org/10.1002/14356007.a14_381.pub2

7. Castro RHR, Gouvêa D. Sintering and nanostability: the thermodynamic perspective. J Am Ceram Soc. 99(4):1105–21. https://doi.org/10.1111/jace.14176

8. Janczarek M, Kowalska E. Defective dopant-free TiO_2 as an efficient visible light-active photocatalyst. Catalysts. 2021;11(8):978. https://doi.org/10.3390/catal11080978

9. Nassau K. The physics and chemistry of color: the 15 mechanisms. In: Shevell SK, editor. The Science of Color: Second Edition, 2nd ed. Elsevier Ltd; 2003:247–80. https://doi.org/10.1016/B978-044451251-2/50008-8

10. Serpone N. Is the band gap of pristine TiO_2 narrowed by anion- and cation-doping of titanium dioxide in second-generation photocatalysts? J Phys Chem B. 2006;110(48):24287–93. https://doi.org/10.1039/b006527g

11. Livraghi S, Chiesa M, Paganini MC, Giamello E. On the nature of reduced states in titanium dioxide as monitored by electron paramagnetic resonance. I: The anatase case. J Phys Chem C. 2011;115(51):25413–21. https://doi.org/10.1021/jp5070374

12. Chiesa M, Paganini MC, Livraghi S, Giamello E. Charge trapping in TiO_2 polymorphs as seen by Electron Paramagnetic Resonance spectroscopy. Phys Chem Chem Phys. 2013;15(24):9435–47. https://doi.org/10.1039/c3cp50658d

13. Mohajernia S, Andryskova P, Zoppellaro G, Hejazi S, Kment S, Zboril R, et al. Influence of Ti^{3+} defect-type on heterogeneous photocatalytic H_2 evolution activity of TiO_2. J Mater Chem A Mater. 2020;8(3):1432–42. https://doi.org/10.1039/c9ta10855f

14. Li Y, Peng YK, Hu L, Zheng J, Prabhakaran D, Wu S, et al. Photocatalytic water splitting by $N-TiO_2$ on MgO (111) with exceptional quantum efficiencies at elevated temperatures. Nat Commun. 2019;10(1):1–10. https://doi.org/10.1038/s41467-019-12385-1

15. D'Arienzo M, Carbajo J, Bahamonde A, Crippa M, Polizzi S, Scotti R, et al. Photogenerated defects in shape-controlled TiO_2 anatase nanocrystals: A probe to evaluate the role of crystal facets in photocatalytic processes. J Am Chem Soc. 2011;133(44):17652–61. https://doi.org/10.1021/ja204838s

16. Anpo M, Che M, Fubini B, Garrone E, Giamello E, Paganini MC. Generation of superoxide ions at oxide surfaces. Top Catal. 1999;8(3–4):189–98. https://doi.org/10.1023/a:1019117328935

17. Bouziani A, Yahya M, Naciri Y, Hsini A, Khan MA, Sillanpaa M, et al. Development of polyaniline coated titania-hematite composite with enhanced photocatalytic activity under sun-like irradiation. Surf Interfaces. 2022;34:102328. https://doi.org/10.1016/j.surfin.2022.102328

18. Xing M, Fang W, Nasir M, Ma Y, Zhang J, Anpo M. Self-doped Ti^{3+}-enhanced TiO_2 nanoparticles with a high-performance photocatalysis. J Catal. 2013;297:236–43. https://doi.org/10.1016/j.jcat.2012.10.014

19. Saroj S, Singh L, Singh SV. Solution-combustion synthesis of anion (iodine) doped TiO_2 nanoparticles for photocatalytic degradation of Direct Blue 199 dye and regeneration of used photocatalyst. J Photochem Photobiol A Chem. 2020;396:112532. https://doi.org/10.1016/j.jphotochem.2020.112532

20. Zhang Q, Li Y, Ackerman EA, Gajdardziska-Josifovska M, Li H. Visible light responsive iodine-doped TiO_2 for photocatalytic reduction of CO_2 to fuels. Appl Catal A Gen. 2011;400(1–2):195–202. https://doi.org/10.1016/j.apcata.2011.04.032

21. Derrick MR, Stulik D, Landry JM. Infrared spectroscopy in Conservation Science. 1st ed. Los Angeles: Getty Conservation Institute; 1999 https://doi.org/10.1017/CBO9781107415324.004

22. Compagnoni M, Villa A, Bahdori E, Morgan DJ, Prati L, Dimitratos N, et al. Surface probing by spectroscopy on titania-supported gold nanoparticles for a photoreductive application. Catalysts. 2018;8(12):623. https://doi.org/10.3390/catal8120623

23. Ramis G, Busca G, Lorenzelli V. Low-temperature CO_2 adsorption on metal oxides: spectroscopic characterization of some weakly adsorbed species. Mater Chem Phys. 1991;29(1–4):425–35. https://doi.org/10.1016/0254-0584(91)90037-U

24. Mino L, Spoto G, Ferrari AM. CO_2 capture by TiO_2 anatase surfaces: a combined DFT and FTIR study. J Phys Chem C. 2014;118:25016–26. https://doi.org/10.1021/jp507443k

25. Martra G. Lewis acid and base sites at the surface of microcrystalline TiO_2 anatase: relationships between surface morphology and chemical behaviour. Appl Catal A Gen. 2000;200:275–85. https://doi.org/10.1016/S0926-860X(00)00641-4

26. Mino L, Zecchina A, Martra G, Mario Rossi A, Spoto G. A surface science approach to TiO_2 P25 photocatalysis : an in situ FTIR study of phenol photodegradation at controlled water coverages from sub-monolayer to multilayer. Appl Catal B. 2016;196:135–41. https://doi.org/10.1016/j.apcatb.2016.05.029

27. He H, Zapol P, Curtiss LA. A theoretical study of CO_2 anions on anatase (101) surface. J Phys Chem C. 2010;114(49):21474–81. https://doi.org/10.1021/jp106579b

28. Liu L, Zhao H, Andino JM, Li Y. Photocatalytic CO_2 reduction with H_2O on TiO_2 nanocrystals: comparison of anatase, rutile, and brookite polymorphs and exploration of surface chemistry. ACS Catal. 2012;2(8):1817–28. https://doi.org/10.1021/cs300273q

29. Raskó J, Solymosi F. Infrared spectroscopic study of the photoinduced activation of CO_2 on TiO_2 and Rh/TiO_2 catalysts. J Phys Chem. 1994;98(29):7147–52. https://doi.org/10.1021/j100080a009

30. Liu L, Zhao C, Li Y. Spontaneous dissociation of CO_2 to CO on defective surface of $Cu(I)/TiO_{2-x}$ nanoparticles at room temperature. J Phys Chem C. 2012;116(14):7904–12. https://doi.org/10.1021/jp300932b

31. Liu L, Li Y. Understanding the reaction mechanism of photocatalytic reduction of CO_2 with H_2O on TiO_2-based photocatalysts: a review. Aerosol Air Qual Res. 2014;14(2):453–69. https://doi.org/10.4209/aaqr.2013.06.0186

32. Nowotny J, Bak T, Nowotny MK, Sheppard LR. Titanium dioxide for solar-hydrogen II. Defect chemistry. Int J Hydrogen Energy. 2007;32(14):2630–43. https://doi.org/10.1016/j.ijhydene.2006.09.005

33. Nowotny MK, Bogdanoff P, Dittrich T, Fiechter S, Fujishima A, Tributsch H. Observations of p-type semiconductivity in titanium dioxide at room temperature. Mater Lett. 2010;64(8):928–30. https://doi.org/10.1016/j.matlet.2010.01.061

34. Wang S, Pan L, Song JJ, Mi W, Zou JJ, Wang L, et al. Titanium-defected undoped anatase TiO_2 with p-type conductivity, room-temperature ferromagnetism, and remarkable photocatalytic performance. J Am Chem Soc. 2015;137(8):2975–83. https://doi.org/10.1021/ja512047k

35. Gandelman H, da Silva AL, Ramos B, Gouvêa D. Interface excess on Sb-doped TiO_2 photocatalysts and its influence on photocatalytic activity. Ceram Int. 2021;47(1):619–25. https://doi.org/10.1016/j.ceramint.2020.08.169

36. da Silva AL, Muche DNF, Caliman LB, Bettini J, Castro RHR, Navrotsky A, et al. TiO_2 surface engineering to improve nanostability: the role of interface segregation. J Phys Chem C. 2019;123(8):4949–60. https://doi.org/10.1021/acs.jpcc.8b12160

37. Liao X, Pu Y, Zhu D. Synergistic effect of co-doping of nanosized ZnO and Nb_2O_5 on the enhanced nonlinear coefficient of TiO_2 varistor with low breakdown voltage. J Alloys Compd. 2021;886:9. https://doi.org/10.1016/j.jallcom.2021.161170

38. Peng F, Zhu D, Yan Q, Li Y. Influence of GeO_2 on the microstructure and electrical properties of TiO_2–Nb_2O_5–Ho_2O_3 –SiO_2 varistors. Mater Chem Phys. 2020;243:8. https://doi.org/10.1016/j.matchemphys.2020.122638

39. Bak T, Chu D, Francis AR, Li W, Nowotny J. Concentration of electrons at grain boundaries in TiO_2 (rutile): impact on charge transport and reactivity. Catal Today. 2014;224:200–8. https://doi.org/10.1016/j.cattod.2013.11.039

40. Green J, Carter E, Murphy DM. Interaction of molecular oxygen with oxygen vacancies on reduced TiO_2: site specific blocking by probe molecules. Chem Phys Lett. 2009;477(4–6):340–4. https://doi.org/10.1016/j.cplett.2009.07.002

41. Howe RF, Grätzel M. EPR study of hydrated anatase under UV irradiation. J Phys Chem. 1987;91(14):3906–9. https://doi.org/10.1021/j100298a035

42. Xiong LB, Li JL, Yang B, Yu Y. Ti^{3+} in the surface of titanium dioxide: generation, properties and photocatalytic application. J Nanomater. 2012;2012:13. https://doi.org/10.1155/2012/831524

43. Yang L, Yu LE, Ray MB. Photocatalytic oxidation of paracetamol: dominant reactants, intermediates, and reaction mechanisms. Environ Sci Technol. 2009;43(2):460–5. https://doi.org/10.1021/es8020099

44. Long R, Liu J, Prezhdo OV. Unravelling the effects of grain boundary and chemical doping on electron–hole recombination in $CH_3NH_3PbI_3$ perovskite by time-domain atomistic simulation. J Am Chem Soc. 2016;138(11):3884–90. https://doi.org/10.1021/jacs.6b00645

SUPPORTING INFORMATION

Additional supporting information can be found online in the Supporting Information section at the end of this article.